CHEMISTRY OF MATERIALS

pubs.acs.org/cm

Article

Flexible 2D Boron Imidazolate Framework for Polysulfide Adsorption in Lithium−Sulfur Batteries

Soumyodip Banerjee, Xu Han, Maxime A. Siegler, Elisa M. Miller, Nicholas M. Bedford, Brandon C. Bukowski, and V. Sara Thoi*

Cite This: *Chem. Mater.* 2022, 34, 10451−10458

Read Online

ACCESS | Metrics & More | Article Recommendations | Supporting Information

ABSTRACT: The "polysulfide shuttle," a process initiated by the dissolution of polysulfides, is recognized to be one of the major failure mechanisms of lithium−sulfur (Li−S) batteries. Much research effort has been dedicated toward efficient cathode additives and host materials to suppress the leaching of polysulfide species. Herein, we report a new 2D metal−organic framework constituted by a tritopic ligand, boron imidazolate ($[BH(Im)_3]^-$, Im = imidazole), and Co^{2+} ions for lithium polysulfide adsorption. The cobalt imidazolate framework (CoN_6-BIF) contains octahedrally coordinated Co centers that form two-dimensional layers in the *a*,*b* plane. Composite cathodes containing CoN_6-BIF exhibited high sulfur utilization and capacity retention, resulting in improved specific capacity and cycle life compared to sulfur/carbon controls. Density functional theory (DFT) calculations suggest that CoN_6-BIF linkers are rotationally flexible, allowing the framework to accommodate polysulfide in the expanded pores. This unusual property of BIFs opens up new avenues for exploring flexible metal−organic frameworks (MOFs) and their applications to energy storage.

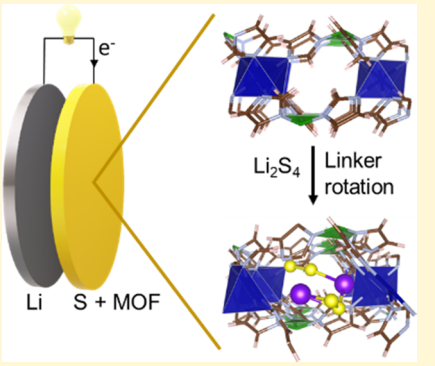

INTRODUCTION

Lithium−sulfur (Li−S) batteries are a promising alternative to existing energy storage technologies. In contrast to the traditional intercalation cathodes in Li-ion batteries, S-based conversion cathodes utilize multielectron redox chemistry that leads to the breaking and formation of covalent S−S bonds. The high theoretical gravimetric energy density of 2680 W h kg^{-1} and the relatively low cost of sulfur make Li−S batteries highly desirable.[1] Despite these advantages, the practical applicability of this technology is severely plagued by the so-called "polysulfide shuttle" phenomenon.[2−4] During the discharge cycle, elemental sulfur is reduced to generate lithium polysulfide species that are soluble in common electrolytes. Polysulfide dissolution results in a loss of active material from the cathode. Furthermore, the dissolved polysulfide species can diffuse to the counter electrode compartment and form an insulating Li_2S precipitate on the Li anode, which increases cell impedance and limits the overall capacity.

To mitigate the polysulfide leaching from the cathode, various carbonaceous materials, including hollow carbon spheres, porous carbon, carbon nanotubes, and graphene, were initially employed as sulfur hosts.[5−12] However, the polysulfide shuttle is still observed due to the low availability of adsorption sites in these materials. Inorganic polar compounds such as metal chalcogenides, nitrides, and carbides contain polar metal−heteroatom bonds, making them good candidates for polysulfide adsorption.[13−20] For instance, Nazar et al. leveraged polar Mn−O bonds in ultrathin MnO_2 nanosheets for polysulfide adsorption and proposed the generation of a surface-bound polythionate intermediate.[14] In another work, W_2C nanoparticles were incorporated into the electrode, which facilitated polysulfide binding through polar interactions.[18] Their high density, however, limits their utility because polysulfides cannot diffuse into the bulk, and only the surface is available for polysulfide binding.

Metal−organic frameworks (MOFs) are a class of organic−inorganic hybrid materials, constituted by organic linkers and metal ions.[4,21−23] Their inherent porous structure provides spatial confinement for the polysulfide species via both physisorption and chemisorption sites.[4,24] The synthetic tunability of these materials allows for facile modulation of the pore environment that can result in higher Li diffusion, faster redox hopping, and more efficient chemical tethering of leached Li_2S_n.[25−34] Additionally, MOFs, such as zeolitic imidazolate frameworks (ZIFs), have demonstrated extraordinary structural flexibility that can be leveraged for polysulfide encapsulation. The importance of linker flexibility in ZIF-8 for correctly predicting adsorption capacity and diffusion has been

Received: August 8, 2022
Revised: October 31, 2022
Published: November 15, 2022

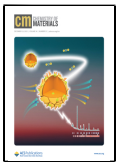

Scheme 1. (a) Synthesis of CoN_6-BIF. (b) Crystal Structure of CoN_6-BIF (B = Green, C = Brown, N = Gray, Co = Blue)

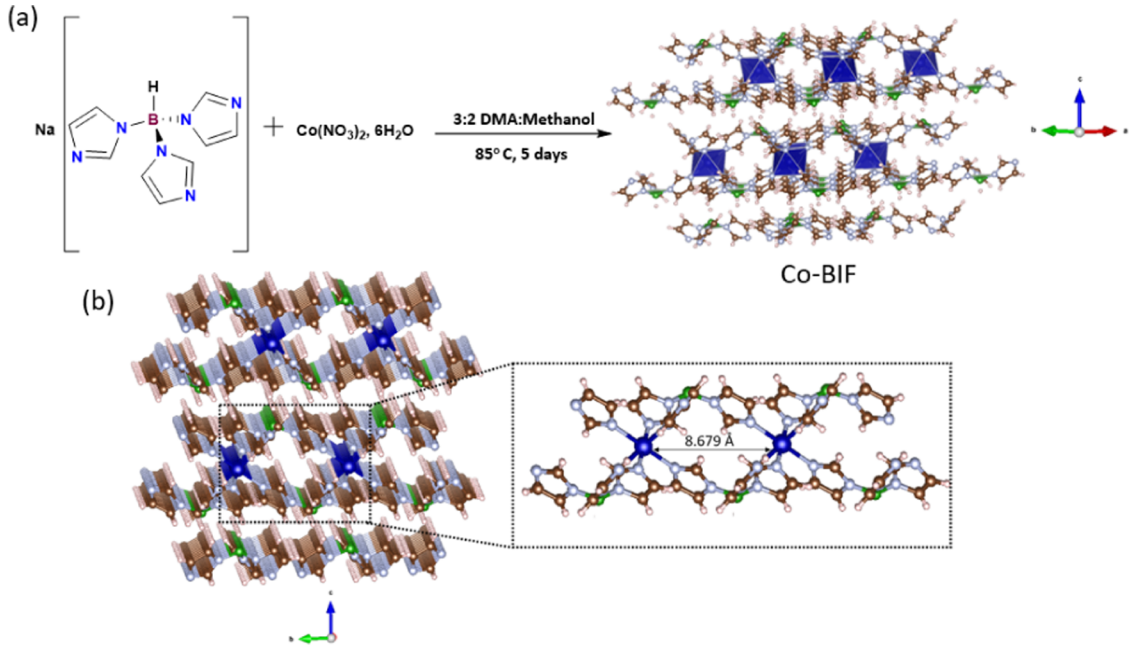

shown by Haldoupis et al.,[35] Coudert,[36] and Formalik et al.[37] among others.[38−41]

Boron imidazolate frameworks (BIFs) are a subclass of MOFs containing M−Im−B (M = metal, Im = imidazole, B = boron) linkage, where imidazole-based linkers serve as a bridging ligand.[42] BIFs with various zeolitic topologies and metal sites have been employed in photo- and electrocatalysis.[43−47] Herein, we synthesized a novel Co-based boron imidazolate framework (CoN_6-BIF) as a flexible porous host for polysulfides. Unlike Cu analogues, which form multinuclear metal cages, CoN_6-BIFs are composed of isolated hexacoordinated Co^{2+} centers that arrange in two-dimensional (2D) sheets, generating one-dimensional (1D) channels along the a-direction. The composite cathodes with BIF additives exhibit significantly higher capacity retention over traditional S/C cathodes. Extensive spectroscopic characterization and simulations suggest that this improvement can be attributed to physical confinement and noncovalent interactions of polysulfides in the 2D material. In our density functional theory (DFT) calculations, Co-bound imidazolate linkers can rotate and expand the internal pore volume to accommodate polysulfide adsorption, a fluxionality that is reminiscent of that observed in ZIF-8. Our investigation demonstrates the first example of flexible BIFs and their potential as sulfur hosts for lithium−sulfur batteries.

EXPERIMENTAL SECTION

Synthesis of CoN_6-BIF Powder. In a typical synthesis, ∼50 mg (0.21 mmol) of the $Na[BH(Im)_3]$ was dissolved in 5 ml 3:2 dimethylacetamide: methanol solvent mixture in a 20 ml vial. ∼ 150 mg (0.5 mmol) of $Co(NO_3)_2$, $6H_2O$ was added to the mixture and stirred for 5 minutes to dissolve. Upon completion, the pink powders were washed with 100 mL of (20 mL × 5 times) methanol and soaked in methanol overnight. On the next day, the BIF powder was further washed with 100 mL (20 mL × 5 times) in methanol and soaked overnight. The powder was then air-dried and subjected to powder X-ray diffraction (PXRD). The PXRD pattern perfectly matched the one obtained by simulating the single-crystal data.

Cathode Preparation. The S/C slurry mixtures were prepared with 45% sulfur, 45% Super-P carbon, and 10% poly(vinylidene fluoride) (PVDF) binder. For the CoN_6-BIF cathodes, the BIF powder was activated using a Schlenk line at 170 °C for 3 h under constant vacuum before using it as a cathode additive. We optimized the cathode slurry composition by varying the BIF/Super-P carbon ratio. To prepare the slurry mixture, a calculated amount of the resulting activated BIF powder was physically mixed with S, Super-P carbon, PVDF using a vortex mixer in the presence of three small stainless steel balls for 5 min. After the initial mixing, *N*-methyl-2-pyrrolidinone was added to the mixture and then vortexed for another 30 min. The homogeneous slurry was then cast onto 12.7 mm preweighed carbon paper disks and was dried in a vacuum oven at 80 °C overnight. After drying, the cathodes were further weighed to determine the sulfur loading and transferred to an Ar-filled glovebox.

Coin Cell Preparation and Cycling. CR 2032-type coin cells were assembled in an Ar-filled glovebox using a preweighed cathode, two Celgard separators, two stainless steel spacers, a spring (TOB New Energy), and a mechanically polished Li anode (MTI Corporation). The electrolyte was prepared by dissolving 1 M bis(trifluoromethanesulfonyl)imide lithium (LiTFSI) and 2 wt % lithium nitrate in a 1:1 mixture of 1,2-dimethoxyethane (DME) and 1,3-dioxolane (DOL); 60 μL of electrolyte per mg of S was used to ensure reproducible cycling. Next, the freshly prepared cells were cycled galvanostatically with a MicroNanoTools battery analyzer (MNT-BA-5V) after resting for 8 h.

DFT Calculations. Static DFT calculations were performed using the Vienna Ab initio Simulation Package (VASP).[48−51] The PBE functional[52] was used with Grimme's D3 dispersion corrections (PBE-D3).[53] A cutoff energy of 550 eV was used along with a convergence criterion of 0.05 eV $Å^{-1}$. The projector augmented wave (PAW) pseudopotentials were used.[54] All calculations were performed spin-polarized due to the presence of Co in the framework.

Adsorbate species (Li_2S, Li_2S_2, Li_2S_4) were relaxed in a 12 Å × 11 Å × 10 Å box. The experimental CoN_6-BIF CIF (crystallographic information file) was fully relaxed, and the *a*,*b* lattice vectors decreased from 8.68 to 8.42 Å (3% contraction) and the *c* lattice vector changed by less than 0.01 Å. Co ions were given a high initial spin using the MAGMOM tag in VASP, as higher Co spin states were found to be more energetically favorable. Adsorption calculations were performed both on the CoN_6-BIF single unit cell and a 2 × 2 × 1 CoN_6-BIF supercell. The supercell lattice was relaxed, and the *a*,*b*

https://doi.org/10.1021/acs.chemmater.2c02324
Chem. Mater. 2022, 34, 10451−10458

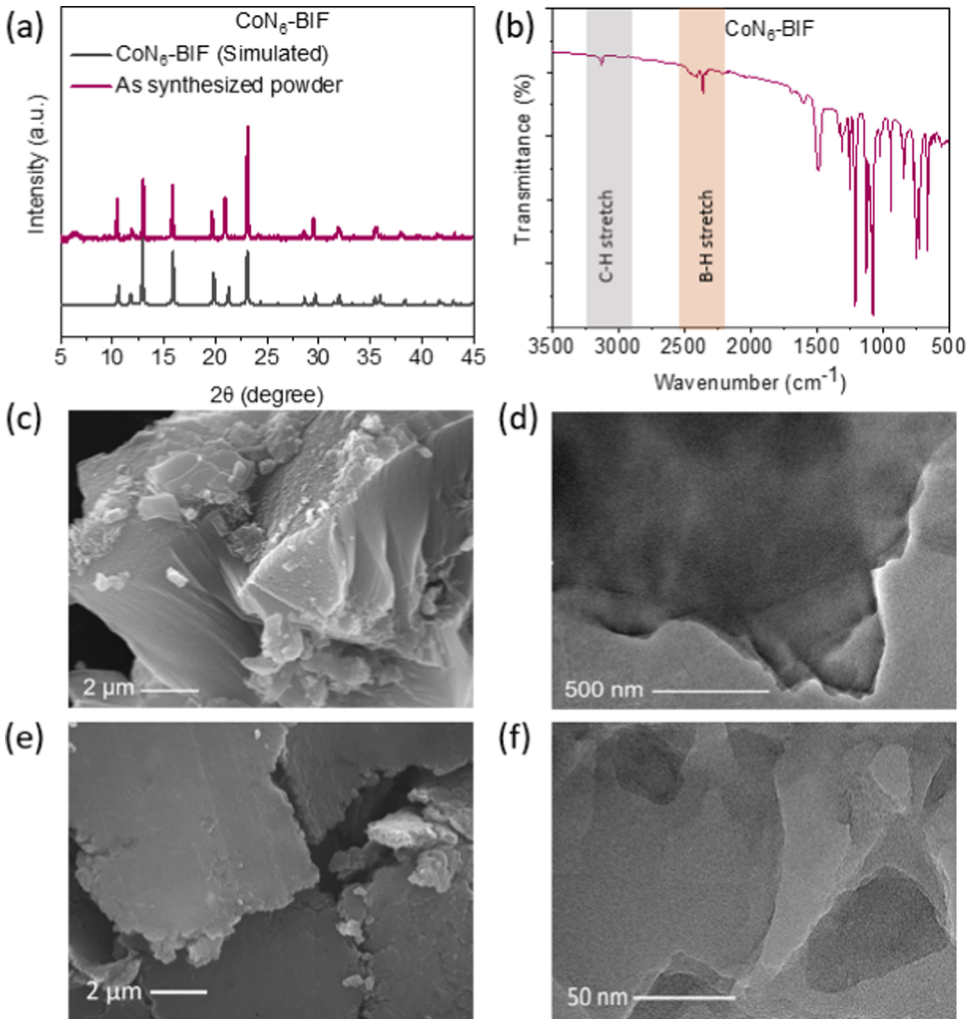

Figure 1. (a) PXRD of the CoN_6-BIF powder (pink) and comparison with simulated data (black), (b) infrared (IR) spectrum of CoN_6-BIF, scanning electron micrographs of (c) CoN_6-BIF and (e) exfoliated CoN_6-BIF, and transmission electron micrographs of (d) CoN_6-BIF and (f) exfoliated CoN_6-BIF.

lattice vectors increased to 8.45 Å, while the *c* lattice vector changed by less than 0.01 Å. For single-unit-cell simulations, a 2 × 2 × 2 γ centered *K*-point grid was used. Due to the size of the supercell, only the γ point was sampled. We performed a single-point calculation on the supercell using a 2 × 2 × 1 γ-centered *K*-point grid and found the total energy to differ by <0.01 eV, and the remaining supercell calculations were performed with a single *K*-point. For the adsorbed species, the unit cell was allowed to relax to account for expansion of the vdW volume during adsorption. Adsorption energies were defined according to the following equation

$$E_{ads} = E_{Li_2S_n+BIF} - E_{BIF} - E_{Li_2S_n}(g)$$

where $E_{Li_2S_n}(g)$ is the potential energy of the polysulfide in vacuum, E_{BIF} is the potential energy of a vacant CoN_6-BIF framework, and $E_{Li_2S_n + BIF}$ is the potential energy of the adsorbed state.

Ab Initio Molecular Dynamics (AIMD). To account for the flexibility of the framework under ambient conditions, we performed ab initio molecular dynamics (AIMD) simulations of adsorbed lithium polysulfides and generate candidate structures to assist in finding the global lowest energy adsorbed structure. All AIMD was performed spin-polarized with the same 550 eV cutoff energy. For both the unit cell and the 2 × 2 × 1 supercell, we first used a 0.5 ps temperature ramp from 0 to 300 K with a 1 fs timestep. We then performed 1 ps production runs for the unit cell (0.5 ps for the supercell) at 600 K using a Nosé−Hoover thermostat. The elevated temperature was used to accelerate the motion of the linkers, which was strictly for structural optimization. Six candidate structures were harvested from each AIMD trajectory and chosen based on their potential energy. Each of the six candidate structures was then geometry-optimized using the criteria described above.

Helium Void Fraction Simulations. The helium void fraction of the vacant and adsorption-deformed CoN_6-BIFs was performed via Widom insertion using RASPA 2.0 software.[55] We took the DFT-optimized 2 × 2 × 1 supercell and the DFT-optimized 2 × 2 × 1 supercell with Li_2S_4 adsorbed (Li_2S_4 was removed from the structure) and kept them rigid. Since our aim was to compare the change in accessible pore volume due to linker rotation upon adsorption, it was preferable to keep the structures rigid for this study. We performed 25,000 helium insertions for each void fraction calculation.

RESULTS AND DISCUSSION

In this work, a Co boron imidazolate framework was synthesized by solvothermal self-assembly of Co^{2+} ions and a previously published tripodal boron imidazolate linker, Na-$[BH(Im)_3]$[56] (where Im = imidazole) to form $Co[BH(Im)_3]_2$ (CoN_6-BIF, Scheme 1a). Single crystals of BIF were formed in the presence of a modulator, 1,2,3-triazole. Single-crystal X-ray diffraction showed that boron imidazolate, $[BH(Im)_3]^-$, serves as a μ3-bridging ligand between three different Co^{2+} centers, generating a 2D framework composed of CoN_6 polyhedra

https://doi.org/10.1021/acs.chemmater.2c02324
Chem. Mater. 2022, 34, 10451−10458

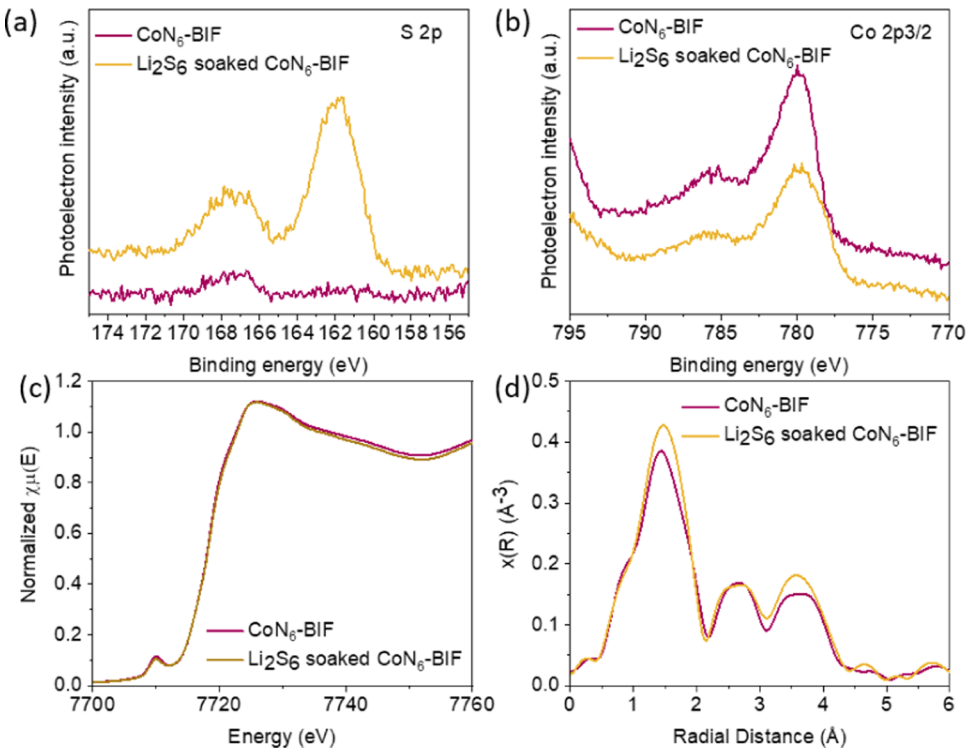

Figure 2. High-resolution XPS of (a) S 2p and (b) Co $2p_{3/2}$, (c) Co K-edge X-ray near-edge absorption spectrum (XANES), and (d) extended X-ray absorption fine structure (EXAFS) of CoN_6-BIF (pink) and Li_2S_6 soaked CoN_6-BIF (yellow).

(Scheme 1a). The 2D layers form an extended structure along the c-direction. Furthermore, 1D channels with a Co−Co distance of 8.979 Å extend in the a-direction (Scheme 1b). The polycrystalline powder was synthesized in the absence of any modulator. The powder X-ray diffraction (PXRD) pattern of the as-synthesized powder material aligns with the simulated diffraction pattern of the single-crystal structure (Figure 1a). Confirming its two-dimensionality, the framework can be exfoliated using ultrasonication (see the Experimental Details in the Supporting Information, SI). The PXRD intensity along (002) and (004) directions increased in the exfoliated framework (Figure S1), indicating a preferential orientation.

In addition, the infrared (IR) absorption spectrum (Figure 1b) of the BIF powder shows the expected B−H feature at ∼2360 cm^{-1}. The thermal stability of the material was also evaluated by conducting thermogravimetric analysis (TGA) under Ar. Owing to the extended structure, CoN_6-BIF exhibits a much higher decomposition temperature (Figure S2) compared to previously reported boron imidazolate cages. Upon conducting Brunauer−Emmett−Teller (BET) surface area analysis, CoN_6-BIF shows 20.28 $m^2\ g^{-1}$ (Figure S3a) with a pore width of 8.82 Å (Figure S3b). The pore width is consistent with the 1D channels observed in the crystal structure (Scheme 1b). Finally, scanning electron microscopy (SEM) and transmission electron microscopy (TEM) showed that while the primary particles of CoN_6-BIF do not possess any distinct shape, (Figure 1c), evidence of 2D stacking can be seen (Figure 1c,d). These observations were corroborated by SEM and TEM images of the exfoliated CoN_6-BIF (Figure 1e,f).

To examine the polysulfide-capturing ability of CoN_6-BIF, 10 mg of the BIF powder was soaked with 1 mL of 10 mM Li_2S_6 in a 1:1 DOL/DME solution overnight. Upon soaking, the pink CoN_6-BIF powders turned brown (Figure S4a). After removing the excess solvent, the material was washed thoroughly with a 1:1 DOL:DME and dried under vacuum. The powder was subsequently subjected to PXRD, Raman, and X-ray photoelectron spectroscopy (XPS). Despite the color change, the unchanged PXRD pattern (Figure S4b) and Raman features (Figure S4c) indicate a similar crystallographic orientation and molecular structure of BIF after soaking. We also compared the XPS spectra of the sulfur-soaked BIF with the parent material to understand the nature of the interactions between the Co centers and the polysulfide (Figures 2a,b and S5). The polysulfide-soaked CoN_6-BIF showed a feature centered at 161.95 eV, which was absent in the parent BIF (Figure 2a, yellow). This feature corresponded to the terminal S of the polysulfide chain[57] and, therefore, was indicative of the polysulfide infiltration into the framework. We noted that the higher binding energy S peak (∼167 eV) was likely due to SO_X surface contamination from the glovebox. Interestingly, no shift of the Co $2p_{3/2}$ feature was observed in our XPS after polysulfide soaking (Figure 2b), which suggested that saturated Co centers were unable to interact with the polysulfides.

X-ray absorption (EXAFS) spectroscopy was conducted on both the parent BIF and the polysulfide-soaked sample to gain deeper insights into the polysulfide absorption mechanism. (Figures 2c,d and S6) The Co K-edge X-ray near-edge absorption spectrum (XANES) of the parent BIF shows a similar E_0 value as other Co^{2+}-containing materials (Figure 2c, pink). No shift of the E_0 value was observed after polysulfide soaking, which suggests that the Co oxidation state remains similar (Figure 2c, yellow). Finally, the extended X-ray absorption fine structure (EXAFS) of CoN_6-BIF exhibits a sharp feature centered at 1.44 Å (Figure 2d, not corrected for the phase), which corresponds to the Co−N bond. A similar EXAFS feature was observed in the polysulfide-soaked CoN_6-BIF, indicating that the primary coordination sphere around

https://doi.org/10.1021/acs.chemmater.2c02324
Chem. Mater. 2022, 34, 10451−10458

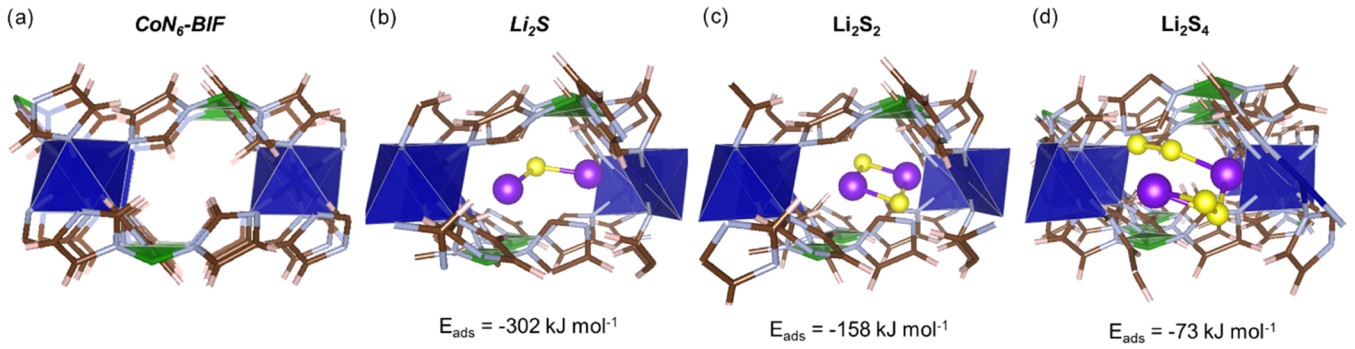

Figure 3. Lowest energy adsorbate configurations and adsorption energies for lithium polysulfides in CoN_6-BIF. The imidazolate linkers rotate to accommodate lithium polysulfide adsorption. Blue polyhedral is Co, light blue is N, green polyhedral is B, brown is C, yellow is S, and purple is Li. Note that the surrounding CoN_6-BIF framework has been truncated for clarity. Additional adsorption configurations are provided in the Supporting Information.

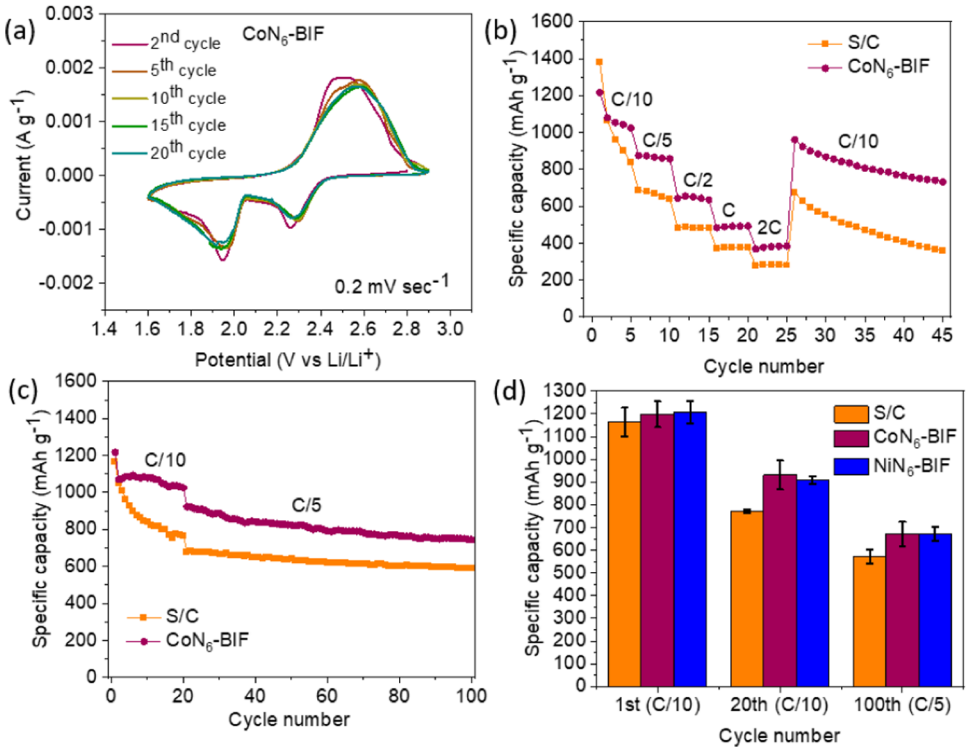

Figure 4. (a) Coin cell cyclic voltammograms in the presence of the 15% CoN_6-BIF cathode additive, (b) variable C-rate cycling comparison in the absence (orange) and presence (pink) of the CoN_6-BIF additive in the cathode, (c) long-term cycling data at C/10 (20 cycles) and C/5 (80 cycles) in the absence (orange) and presence (pink) of CoN_6-BIF in the cathode, and (d) cycling capacity comparison in the absence of any additive (orange) and in the presence of the CoN_6-BIF additive (pink) and the NiN_6-BIF additive (blue) in the cathode. The average S-loading in CoN_6-BIF is 1.463 ± 0.193 mg.

Co is largely unchanged. A small increase in magnitude is noted, perhaps due to minor Co−N reordering upon the inclusion of Li_2S_6. Higher order coordination spheres are also present and similar between the parent BIF and S-loaded materials, with a slight increase in magnitude for the third coordination sphere, again likely to a minor amount of linker reordering. These XANES and EXAFS observations are consistent with the XPS data, leading us to propose that polysulfides are likely physically confined in the framework and not covalently attached.

We performed ab initio simulations of polysulfide adsorption into the CoN_6-BIF framework to gain molecular-level insights into polysulfide adsorption. We found that polysulfides up to Li_2S_4 adsorb favorably into the CoN_6-BIF micropores. For all polysulfides considered, adsorption into the van der Waals layer was less favorable than that into the micropores, even when accounting for volume expansion of the van der Waals layer (Figure S7). Adsorption energies were more exothermic for a 2 × 2 × 1 CoN_6-BIF supercell, likely due to the additional flexibility allowed for the linkers in the larger model. The Li_2S adsorption energy (−302 kJ mol^{-1}) was more exothermic than the Li_2S_2 adsorption energy (−158 kJ mol^{-1}), which in turn was more exothermic than the Li_2S_4 adsorption energy (−73 kJ mol^{-1}, Figure 3). This series is reasonable, as each additional sulfur increases the size of the adsorbate and further strains the framework. As Li_2S_4 adopts a linear sulfur configuration, we hypothesize that larger polysulfides are also able to be adsorbed without significant additional strain. For all

https://doi.org/10.1021/acs.chemmater.2c02324
Chem. Mater. 2022, 34, 10451−10458

polysulfides, the Li ions were observed to interact more strongly with the imidazole linkers proximal to the Co centers. To quantify the impact of linker rotation and expansion on accessible pore volume, the helium void fraction in the 2 × 2 × 1 supercell increased from 0.7% of the cell volume to 2.2% of the cell volume, a >3 × increase in pore volume after Li_2S_4 adsorption. It is reasonable to expect that when framework flexibility and linker rotation are important, larger models are needed to capture these physical effects.

Intrigued by the polysulfide encapsulation ability of CoN_6-BIF in the solution phase, we employed this novel framework as a cathode additive in the Li−S battery. CoN_6-BIF, S, Super-P carbon, and PVDF polymer binder were physically mixed in NMP to form a slurry mixture. The BIF was incorporated at either 15 or 30% mass by weight. The slurry mixture was uniformly coated onto a carbon paper and dried overnight. These cathodes were assembled into a coin cell using 1 M Li(TFSI) (in 1:1 DOL/DME), 2% $LiNO_3$ as an electrolyte, and Li foil as a counter electrode and subjected to various electrochemical tests (Figure S8 and S9). Compared to the 30 wt % BIF composite cathodes, cathodes with 15% CoN_6-BIF exhibit a higher overall capacity that is maintained over long-term cycling at a charge/discharge rate of C/2 (Figure S8b). The cathodes with 15% CoN_6-BIF exhibit stable sulfur utilization (Figure 4a) during coin cell cycling voltammetry experiments compared to the S/C counterparts (Figure S9). In rate capability testing, coin cells were cycled at various C-rates (C/10 to 2C, five cycles in each C-rate). The cathodes comprising the CoN_6-BIF additive show a smaller capacity fade during initial cycles (at C/10 and C/5) and higher recyclability compared to 45% S/C cathodes when cycled back to C/10 (Figure 4b). Despite a similar initial capacity (1162 mAh g^{-1}) for 45% S/C cathodes, a rapid capacity fade (592 mAh g^{-1} after 80 cycles at C/5) is observed (Figure 4c). In contrast, the cathodes with the 15% BIF additive retain reasonable capacity (751 mAh g^{-1} after 80 cycles at C/5) even after 100 cycles (Figure 4c).

We also evaluated the influence of different transition metal centers on cycling performance. To that end, an isostructural NiN_6-BIF was synthesized and employed as a cathode additive (Figure S10). The resulting light blue powder exhibits a similar powder pattern as CoN_6-BIF, indicating a comparable structure (Figure S10a). SEM shows that NiN_6-BIF exhibits an unusual cylindrical morphology (Figure S10e,f). Despite the different metal identity, NiN_6-BIF shows identical capacity retention as CoN_6-BIF over long-term cycling (Figures 4d and S11). These observations further confirm that enhancements in battery cycling performance are likely due to physical confinement in the framework as opposed to metal coordination.

CONCLUSIONS

In summary, we report a flexible 2D layered metal−organic framework composed of octahedral CoN_6 nodes and boron imidazolate $[BH(Im)_3]^-$ linkers. We leverage the unique structural features of this 2D framework to adsorb polysulfides and suppress the shuttle phenomenon, a commonly recognized failure mechanism of Li−S batteries. Extensive ex situ X-ray spectroscopic characterization methods have been conducted to understand the nature of the interaction between our BIF and polysulfide species. Unlike the Lewis acid−base interaction[34] observed in the frameworks with open metal sites, we hypothesize that encapsulation of polysulfides into the micropores plays a major role to immobilize the polysulfide in our BIF as shown through our ab initio simulations. We found that the flexibility of the $[BH(Im)_3]^-$ linkers led to pore expansion upon adsorption, which has also been observed in ZIF-8. Spatial confinement in the framework discourages the polysulfide leaching and therefore promotes cycling stability when these frameworks are employed as a cathode additive in the Li−S battery. Further synthetic explorations are underway to install ionic and electronic conduction pathways for improved rate capability. This investigation encourages the discovery of new boron imidazolate frameworks and their application in electrochemical energy storage.

ASSOCIATED CONTENT

Supporting Information

The Supporting Information is available free of charge at https://pubs.acs.org/doi/10.1021/acs.chemmater.2c02324.

Additional experimental details; synthetic procedure; electrochemical data (PDF)
Crystallographic data (CIF)
DFT-calculated CIF structures (ZIP)

AUTHOR INFORMATION

Corresponding Author

V. Sara Thoi − *Department of Chemistry, Johns Hopkins University, Baltimore, Maryland 21218, United States; Department of Materials Science and Engineering, Johns Hopkins University, Baltimore, Maryland 21218, United States;* orcid.org/0000-0003-0896-4077; Email: sarathoi@jhu.edu

Authors

Soumyodip Banerjee − *Department of Chemistry, Johns Hopkins University, Baltimore, Maryland 21218, United States*

Xu Han − *Department of Chemistry, Johns Hopkins University, Baltimore, Maryland 21218, United States*

Maxime A. Siegler − *Department of Chemistry, Johns Hopkins University, Baltimore, Maryland 21218, United States;* orcid.org/0000-0003-4165-7810

Elisa M. Miller − *Chemistry and Nanoscience Center, National Renewable Energy Laboratory, Golden, Colorado 80401, United States;* orcid.org/0000-0002-7648-5433

Nicholas M. Bedford − *School of Chemical Engineering, University of New South Wales, Sydney, New South Wales 2052, Australia;* orcid.org/0000-0002-4424-7094

Brandon C. Bukowski − *Department of Chemical and Biomolecular Engineering, Johns Hopkins University, Baltimore, Maryland 21218, United States;* orcid.org/0000-0002-2626-8908

Complete contact information is available at: https://pubs.acs.org/10.1021/acs.chemmater.2c02324

Notes

The authors declare no competing financial interest.

ACKNOWLEDGMENTS

The authors acknowledge the support of the National Science Foundation for the CAREER Award (DMR-1945114). S.B. also thanks the William Hooper Grafflin Fellowship from the Department of Chemistry. The authors are grateful to Jackson Davis and Dr. Natalia Drichko at Johns Hopkins University for

their assistance in Raman spectroscopy. We thank Dr. Caitlin Quinn (Department of Chemistry and Biochemistry, University of Delaware) for solid-state NMR spectroscopy. Ian Dillingham and Rasha Anayah are also acknowledged for their assistance in nitrogen isotherm measurements and training in battery preparation, respectively. The authors also thank Carter Gerke for his assistance in scanning electron microscopy. This research used the 10-ID-B Beamline of the Advanced Photon Source, a U.S. Department of Energy (DOE) Office of Science User Facility operated for the DOE Office of Science by Argonne National Laboratory under Contract No. DE-AC02-06CH11357. 10-ID-B is operated by the Materials Research Collaborative Access (MRCAT) supported by the Department of Energy and the MRCAT member institutions. B.C.B. acknowledges the Advanced Research Computing at Hopkins (ARCH) core facility (rockfish.jhu.edu), which is supported by the National Science Foundation (NSF) grant number OAC 1920103. The authors thank Dr. Joshua Wright for assistance with XAS experimentation. E.M.M. performed the XPS at NREL and thanks the National Renewable Energy Laboratory, operated by Alliance for Sustainable Energy, LLC, for the U.S. Department of Energy (DOE) under Contract No. DE-AC36-08GO28308. Funding is provided by the Solar Photochemistry Program, Division of Chemical Sciences, Geosciences, and Biosciencse, Office of Basic Energy Sciences, U.S. Department of Energy. The views expressed in the article do not necessarily represent the views of the DOE or the U.S. Government. The U.S. Government retains and the publisher, by accepting the article for publication, acknowledges that the U.S. Government retains a nonexclusive, paid-up, irrevocable, worldwide license to publish or reproduce the published form of this work or allow others to do so, for U.S. Government purposes.

REFERENCES

(1) Bruce, P. G.; Freunberger, S. A.; Hardwick, L. J.; Tarascon, J. M. LigO2 and LigS Batteries with High Energy Storage. *Nat. Mater.* **2012**, *11*, 19−29.

(2) Ji, X.; Lee, K. T.; Nazar, L. F. A Highly Ordered Nanostructured Carbon-Sulphur Cathode for Lithium-Sulphur Batteries. *Nat. Mater.* **2009**, *8*, 500−506.

(3) Yang, Y.; Zheng, G.; Cui, Y. Nanostructured Sulfur Cathodes. *Chem. Soc. Rev.* **2013**, *42*, 3018−3032.

(4) Baumann, A. E.; Burns, D. A.; Liu, B.; Thoi, V. S. Metal-Organic Framework Functionalization and Design Strategies for Advanced Electrochemical Energy Storage Devices. *Commun. Chem.* **2019**, *2*, 1−14.

(5) Jayaprakash, N.; Shen, J.; Moganty, S. A.; Corona, A.; Archer, L. A. Porous Hollow Carbon@Sulfur Composites for High-Power Lithium−Sulfur Batteries. *Angew. Chem., Int. Ed.* **2011**, *50*, 5904−5908.

(6) Liang, C.; Dudney, N. J.; Howe, J. Y. Hierarchically Structured Sulfur/Carbon Nanocomposite Material for High-Energy Lithium Battery. *Chem. Mater.* **2009**, *21*, 4724−4730.

(7) He, G.; Evers, S.; Liang, X.; Cuisinier, M.; Garsuch, A.; Nazar, L. F. Tailoring Porosity in Carbon Nanospheres for Lithium−Sulfur Battery Cathodes. *ACS Nano* **2013**, *7*, 10920−10930.

(8) Zheng, S.; Chen, Y.; Xu, Y.; Yi, F.; Zhu, Y.; Liu, Y.; Yang, J.; Wang, C. In Situ Formed Lithium Sulfide/Microporous Carbon Cathodes for Lithium-Ion Batteries. *ACS Nano* **2013**, *7*, 10995−11003.

(9) Ji, L.; Rao, M.; Aloni, S.; Wang, L.; Cairns, E. J.; Zhang, Y. Porous Carbon Nanofiber-Sulfur Composite Electrodes for Lithium/Sulfur Cells. *Energy Environ. Sci.* **2011**, *4*, 5053−5059.

(10) Li, Z.; Jiang, Y.; Yuan, L.; Yi, Z.; Wu, C.; Liu, Y.; Strasser, P.; Huang, Y. A Highly Ordered Meso@Microporous Carbon-Supported Sulfur@Smaller Sulfur Core−Shell Structured Cathode for Li−S Batteries. *ACS Nano* **2014**, *8*, 9295−9303.

(11) Wang, H.; Zhang, C.; Chen, Z.; Liu, H. K.; Guo, Z. Large-Scale Synthesis of Ordered Mesoporous Carbon Fiber and Its Application as Cathode Material for Lithium-Sulfur Batteries. *Carbon* **2015**, *81*, 782−787.

(12) Jung, D. S.; Hoon Hwang, T.; Hoon Lee, J.; Young Koo, H.; Shakoor, R. A.; Kahraman, R.; Nam Jo, Y.; Park, M.-S.; Wook Choi, J. Hierarchical Porous Carbon by Ultrasonic Spray Pyrolysis Yields Stable Cycling in Lithium−Sulfur Battery. *Nano Lett.* **2014**, *14*, 4418−4425.

(13) Evers, S.; Yim, T.; Nazar, L. F. Understanding the Nature of Absorption/Adsorption in Nanoporous Polysulfide Sorbents for the Li−S Battery. *J. Phys. Chem. C* **2012**, *116*, 19653−19658.

(14) Liang, X.; Hart, C.; Pang, Q.; Garsuch, A.; Weiss, T.; Nazar, L. F. A Highly Efficient Polysulfide Mediator for Lithium-Sulfur Batteries. *Nat. Commun.* **2015**, *6*, No. 9994.

(15) Yuan, Z.; Peng, H.-J.; Hou, T.-Z.; Huang, J.-Q.; Chen, C.-M.; Wang, D.-W.; Cheng, X.-B.; Wei, F.; Zhang, Q. Powering Lithium−Sulfur Battery Performance by Propelling Polysulfide Redox at Sulfiphilic Hosts. *Nano Lett.* **2016**, *16*, 519−527.

(16) Wang, H.; Zhang, Q.; Yao, H.; Liang, Z.; Lee, H.-W.; Hsu, P.-C.; Zheng, G.; Cui, Y. High Electrochemical Selectivity of Edge versus Terrace Sites in Two-Dimensional Layered MoS2 Materials. *Nano Lett.* **2014**, *14*, 7138−7144.

(17) Al Salem, H.; Chitturi, V. R.; Babu, G.; Santana, J. A.; Gopalakrishnan, D.; Reddy Arava, L. M. Stabilizing Polysulfide-Shuttle in a Li-S Battery Using Transition Metal Carbide Nanostructures. *RSC Adv.* **2016**, *6*, 110301−110306.

(18) Zhou, F.; Li, Z.; Luo, X.; Wu, T.; Jiang, B.; Lu, L.-L.; Yao, H.-B.; Antonietti, M.; Yu, S.-H. Low Cost Metal Carbide Nanocrystals as Binding and Electrocatalytic Sites for High Performance Li−S Batteries. *Nano Lett.* **2018**, *18*, 1035−1043.

(19) Ren, W.; Xu, L.; Zhu, L.; Wang, X.; Ma, X.; Wang, D. Cobalt-Doped Vanadium Nitride Yolk−Shell Nanospheres @ Carbon with Physical and Chemical Synergistic Effects for Advanced Li−S Batteries. *ACS Appl. Mater. Interfaces* **2018**, *10*, 11642−11651.

(20) Yan, Y.; Li, H.; Cheng, C.; Yan, T.; Gao, W.; Mao, J.; Dai, K.; Zhang, L. Boosting Polysulfide Redox Conversion of Li-S Batteries by One-Step-Synthesized Co-Mo Bimetallic Nitride. *J. Energy Chem.* **2021**, *61*, 336−346.

(21) Howarth, A. J.; Peters, A. W.; Vermeulen, N. A.; Wang, T. C.; Hupp, J. T.; Farha, O. K. Best Practices for the Synthesis, Activation, and Characterization of Metal−organic Frameworks. *Chem. Mater.* **2017**, *29*, 26−39.

(22) Banerjee, S.; Anayah, R. I.; Gerke, C. S.; Sara Thoi, V. From Molecules to Porous Materials: Integrating Discrete Electrocatalytic Active Sites into Extended Frameworks. *ACS Cent. Sci.* **2020**, *6*, 1671−1684.

(23) Zhou, H. C.; Long, J. R.; Yaghi, O. M. Introduction to Metal−Organic Frameworks. *Chem. Rev.* **2012**, *112*, 673−674.

(24) Zheng, Y.; Zheng, S.; Xue, H.; Pang, H. Metal-Organic Frameworks for Lithium-Sulfur Batteries. *J. Mater. Chem. A* **2019**, *7*, 3469−3491.

(25) Baumann, A. E.; Aversa, G. E.; Roy, A.; Falk, M. L.; Bedford, N. M.; Thoi, V. S. Promoting Sulfur Adsorption Using Surface Cu Sites in Metal-Organic Frameworks for Lithium Sulfur Batteries. *J. Mater. Chem. A* **2018**, *6*, 4811−4821.

(26) Baumann, A. E.; Burns, D. A.; Díaz, J. C.; Sara Thoi, V. Lithiated Defect Sites in Zr Metal−Organic Framework for Enhanced Sulfur Utilization in Li−S Batteries. *ACS Appl. Mater. Interfaces* **2019**, *11*, 2159−2167.

(27) Liu, B.; Baumann, A. E.; Thoi, V. S. Modulating Charge Transport in MOFs with Zirconium Oxide Nodes and Redox-Active Linkers for Lithium Sulfur Batteries. *Polyhedron* **2019**, *170*, 788−795.

(28) Baumann, A. E.; Han, X.; Butala, M. M. M.; Thoi, V. S. S. Lithium Thiophosphate Functionalized Zirconium MOFs for Li−S Batteries with Enhanced Rate Capabilities. *J. Am. Chem. Soc.* **2019**, *141*, 17891−17899.

(29) Baumann, A. E.; Downing, J. R.; Burns, D. A.; Hersam, M. C.; Sara Thoi, V. Graphene−Metal−Organic Framework Composite Sulfur Electrodes for Li−S Batteries with High Volumetric Capacity. *ACS Appl. Mater. Interfaces* **2020**, *12*, 37173−37181.
(30) Liu, B.; Sara Thoi, V. Improving Charge Transfer in Metal−Organic Frameworks through Open Site Functionalization and Porosity Selection for Li−S Batteries. *Chem. Mater.* **2020**, *32*, 8450−8459.
(31) Burns, D. A.; Benavidez, A.; Buckner, J. L.; Thoi, V. S. Maleimide-Functionalized Metal-Organic Framework for Polysulfide Tethering in Lithium-Sulfur Batteries. *Mater. Adv.* **2021**, *2*, 2966−2970.
(32) Burns, D. A.; Baumann, A. E.; Bennett, K. J.; Díaz, J. C.; Sara Thoi, V. Chemical Sulfide Tethering Improves Low-Temperature Li−S Battery Cycling. *ACS Appl. Mater. Interfaces* **2021**, *13*, 50862−50868.
(33) Chang, Z.; Qiao, Y.; Wang, J.; Deng, H.; Zhou, H. Two-Dimensional Metal-Organic Framework with Perpendicular One-Dimensional Nano-Channel as Precise Polysulfide Sieves for Highly Efficient Lithium-Sulfur Batteries. *J. Mater. Chem. A* **2021**, *9*, 4870−4879.
(34) Zheng, J.; Tian, J.; Wu, D.; Gu, M.; Xu, W.; Wang, C.; Gao, F.; Engelhard, M. H.; Zhang, J. G.; Liu, J.; Xiao, J. Lewis Acid-Base Interactions between Polysulfides and Metal Organic Framework in Lithium Sulfur Batteries. *Nano Lett.* **2014**, *14*, 2345−2352.
(35) Haldoupis, E.; Watanabe, T.; Nair, S.; Sholl, D. S. Quantifying Large Effects of Framework Flexibility on Diffusion in MOFs: CH4 and CO2 in ZIF-8. *ChemPhysChem* **2012**, *13*, 3449−3452.
(36) Coudert, F.-X. Molecular Mechanism of Swing Effect in Zeolitic Imidazolate Framework ZIF-8: Continuous Deformation upon Adsorption. *ChemPhysChem* **2017**, *18*, 2732−2739.
(37) Formalik, F.; Mazur, B.; Fischer, M.; Firlej, L.; Kuchta, B. Phonons and Adsorption-Induced Deformations in ZIFs: Is It Really a Gate Opening? *J. Phys. Chem. C* **2021**, *125*, 7999−8005.
(38) Fairen-Jimenez, D.; Moggach, S. A.; Wharmby, M. T.; Wright, P. A.; Parsons, S.; Düren, T. Opening the Gate: Framework Flexibility in ZIF-8 Explored by Experiments and Simulations. *J. Am. Chem. Soc.* **2011**, *133*, 8900−8902.
(39) Verploegh, R. J.; Nair, S.; Sholl, D. S. Temperature and Loading-Dependent Diffusion of Light Hydrocarbons in ZIF-8 as Predicted Through Fully Flexible Molecular Simulations. *J. Am. Chem. Soc.* **2015**, *137*, 15760−15771.
(40) Chokbunpiam, T.; Fritzsche, S.; Chmelik, C.; Caro, J.; Janke, W.; Hannongbua, S. Gate Opening, Diffusion, and Adsorption of CO2 and N2 Mixtures in ZIF-8. *J. Phys. Chem. C* **2016**, *120*, 23458−23468.
(41) Bukowski, B. C.; Keil, F. J.; Ravikovitch, P. I.; Sastre, G.; Snurr, R. Q.; Coppens, M. O.*Connecting Theory and Simulation with Experiment for the Study of Diffusion in Nanoporous Solids*; Springer: US, 2021; Vol. *27*. DOI: 10.1007/s10450-021-00314-y.
(42) Zhang, H. X.; Liu, M.; Wen, T.; Zhang, J. Synthetic Design of Functional Boron Imidazolate Frameworks. *Coord. Chem. Rev.* **2016**, *307*, 255−266.
(43) Wan, Y. M.; Hong, Q. L.; Zhang, H. X.; Zhang, J. Synthesis of Supramolecular Boron Imidazolate Frameworks for CO2Photoreduction. *Inorg. Chem.* **2020**, *59*, 17851−17855.
(44) Wen, T.; Zheng, Y.; Zhang, J.; Davey, K.; Qiao, S. Z. Co (II) Boron Imidazolate Framework with Rigid Auxiliary Linkers for Stable Electrocatalytic Oxygen Evolution Reaction. *Adv. Sci.* **2019**, *6*, 1−5.
(45) Shao, P.; Zhou, W.; Hong, Q. L.; Yi, L.; Zheng, L.; Wang, W.; Zhang, H. X.; Zhang, H.; Zhang, J. Synthesis of a Boron−Imidazolate Framework Nanosheet with Dimer Copper Units for CO2 Electroreduction to Ethylene. *Angew. Chem., Int. Ed.* **2021**, *60*, 16687−16692.
(46) Zhang, H. X.; Hong, Q. L.; Li, J.; Wang, F.; Huang, X.; Chen, S.; Tu, W.; Yu, D.; Xu, R.; Zhou, T.; Zhang, J. Isolated Square-Planar Copper Center in Boron Imidazolate Nanocages for Photocatalytic Reduction of CO2 to CO. *Angew. Chem., Int. Ed.* **2019**, *58*, 11752−11756.
(47) Hong, Q. L.; Zhang, H. X.; Zhang, J. Synthesis of Boron Imidazolate Frameworks with Cobalt Clusters for Efficient Visible-Light Driven CO2 Reduction. *J. Mater. Chem. A* **2019**, *7*, 17272−17276.
(48) Kresse, G.; Furthmüller, J. Efficient Iterative Schemes for Ab Initio Total-Energy Calculations Using a Plane-Wave Basis Set. *Phys. Rev. B* **1996**, *54*, 11169−11186.
(49) Kresse, G.; Hafner, J. Norm-Conserving and Ultrasoft Pseudopotentials for First-Row and Transition Elements. *J. Phys.: Condens. Matter* **1994**, *6*, 8245−8257.
(50) Kresse, G.; Hafner, J. Ab Initio Molecular Dynamics for Liquid Metals. *Phys. Rev. B* **1993**, *47*, 558−561.
(51) Kresse, G.; Hafner, J. Ab Initio Molecular-Dynamics Simulation of the Liquid-Metalamorphous- Semiconductor Transition in Germanium. *Phys. Rev. B* **1994**, *49*, 14251−14269.
(52) Perdew, J. P.; Burke, K.; Ernzerhof, M. Generalized Gradient Approximation Made Simple. *Phys. Rev. Lett.* **1996**, *77*, 3865−3868.
(53) Grimme, S. Semiempirical GGA-type Density Functional Constructed with a Long-range Dispersion. *J. Comput. Chem.* **2006**, *27*, 1787−1799.
(54) Blöchl, P. E. Projector Augmented-Wave Method. *Phys. Rev. B* **1994**, *50*, 17953−17979.
(55) Dubbeldam, D.; Calero, S.; Ellis, D. E.; Snurr, R. Q. RASPA: Molecular Simulation Software for Adsorption and Diffusion in Flexible Nanoporous Materials. *Mol. Simul.* **2016**, *42*, 81−101.
(56) Zhang, D. X.; Zhang, H. X.; Li, H. Y.; Wen, T.; Zhang, J. Self-Assembly of Metal Boron Imidazolate Cages. *Cryst. Growth Des.* **2015**, *15*, 2433−2436.
(57) Hu, S.; Yi, M.; Huang, X.; Wu, D.; Lu, B.; Wang, T.; Li, N.; Zhu, Z.; Liu, X.; Zhang, J. Cobalt-Doped Porphyrin-Based Porous Organic Polymer-Modified Separator for High-Performance Lithium-Sulfur Batteries. *J. Mater. Chem. A* **2021**, *9*, 2792−2805.